Fully three-dimensional OSEM-based image reconstruction for Compton imaging using optimized ordering schemes

2010 Phys. Med. Biol. 55 5007

(http://iopscience.iop.org/0031-9155/55/17/009)

Phys. Med. Biol. 55 (2010) 5007–5027 doi:10.1088/0031-9155/55/17/009

Fully three-dimensional OSEM-based image reconstruction for Compton imaging using optimized ordering schemes

Soo Mee Kim[1,2], Jae Sung Lee[1,2,3,4,9], Chun Sik Lee[5], Chan Hyeong Kim[6], Myung Chul Lee[1,2], Dong Soo Lee[1,2,7] and Soo-Jin Lee[8]

[1] Department of Nuclear Medicine and Interdisciplinary Programs in Radiation Applied Life Science Major, College of Medicine, Seoul National University, Seoul, Korea
[2] Institute of Radiation Medicine, Medical Research Center, Seoul National University, Seoul, Korea
[3] Department of Biomedical Sciences, Seoul National University, Seoul, Korea
[4] Department of WCU Brain & Cognitive Sciences, Seoul National University, Seoul, Korea
[5] Department of Physics, Chung-Ang University, Seoul, Korea
[6] Department of Nuclear Engineering, Hanyang University, Seoul, Korea
[7] Department of Molecular Medicine and Biopharmaceutical Sciences, Seoul National University, Seoul, Korea
[8] Department of Electronic Engineering, Paichai University, Daejeon, Korea

E-mail: jaes@snu.ac.kr

Received 25 January 2010, in final form 13 July 2010
Published 11 August 2010
Online at stacks.iop.org/PMB/55/5007

Abstract

Although the ordered subset expectation maximization (OSEM) algorithm does not converge to a true maximum likelihood solution, it is known to provide a good solution if the projections that constitute each subset are reasonably balanced. The Compton scattered data can be allocated to subsets using scattering angles (SA) or detected positions (DP) or a combination of the two (AP (angles and positions)). To construct balanced subsets, the data were first arranged using three ordering schemes: the random ordering scheme (ROS), the multilevel ordering scheme (MLS) and the weighted-distance ordering scheme (WDS). The arranged data were then split into J subsets. To compare the three ordering schemes, we calculated the coefficients of variation (CVs) of angular and positional differences between the arranged data and the percentage errors between mathematical phantoms and reconstructed images. All ordering schemes showed an order-of-magnitude acceleration over the standard EM, and their computation times were similar. The SA-based MLS and the DP-based WDS led to the best-balanced subsets (they provided the largest angular and positional differences for SA- and DP-based arrangements, respectively). The WDS exhibited minimum CVs for both the SA- and DP-based arrangements

[9] Author to whom any correspondence should be addressed.

(the deviation in mean angular and positional differences between the ordered subsets was smallest). The combination of AP and WDS yielded the best results with the lowest percentage errors by providing larger and more uniform angular and positional differences for the SA and DP arrangements, and thus, is probably optimal Compton camera reconstruction using OSEM.

(Some figures in this article are in colour only in the electronic version)

1. Introduction

Current techniques for single-photon imaging in nuclear medicine rely on mechanical collimation to form projection data of the source distribution. Unfortunately, however, the performance of mechanical collimators suffers from a difficulty due to the inverse relationship between detection efficiency and spatial resolution. In contrast, since a Compton camera provides directional information on incoming photons without mechanical collimation based on the relationship between energy transfer and the Compton scattering angle (SA) of gamma rays in a detector, detection efficiency and spatial resolution are no longer bounded by the inverse relationship.

A typical Compton camera system consists of two detectors: a position-sensitive detector with high-energy resolution and a second position-sensitive detector with low-energy resolution (LeBlanc *et al* 1999, Yang *et al* 2001, Lee *et al* 2005, Lee and Lee 2006, An *et al* 2007, Seo *et al* 2008). Valid events are recorded when the photons that reach the first detector are Compton scattered and then totally absorbed in the second detector. The SA increases as a function of the energy deposited in the scatterer. Furthermore, since the directions of the scattered photon are determined by the two detected positions (DPs) in the scatterer and the absorber, the incident directions of emitted photons onto the scatterer can be computed within a conical surface of ambiguity as shown in figure 1(a).

Since information from the Compton camera only concerns the incident gamma ray direction on the conical surface, an inversion method is needed to reconstruct the source distribution. Various methods have been proposed to reconstruct the three-dimensional (3D) source distribution from Compton scattered conical projection data. An extensive overview of existing reconstruction algorithms for a Compton camera is provided in Smith (2005). Due to computational limitations, many algorithms are based on direct analytical methods rather than being based on statistical methods that are usually performed in iterative reconstruction schemes. The simplest reconstruction method is the backprojection of all measured data into the image space through the conical surfaces. The simple backprojection method, however, results in the loss of high-frequency components such as the edges of objects in the reconstructed images. Parra and other researchers investigated the use of series expansion methods in the spherical harmonic domain to directly reconstruct Compton scattered data (Basko *et al* 1998, Parra 2000, Tomitani and Hirasawa 2002, Hirasawa and Tomitani 2003). In these algorithms, however, the noise properties in measured data due to the randomness of emission and detection process cannot be incorporated in the reconstruction procedure (Smith 2005, Qi and Leahy 2006). In this paper we note that, although analytical reconstruction methods for Compton imaging may be useful for achieving reconstructions in clinically acceptable time, statistical methods, such as maximum likelihood expectation maximization (ML-EM or EM) and maximum *a posteriori* (MAP) approaches, which have been proven to be useful for conventional emission computed tomography (ECT), have great potential for

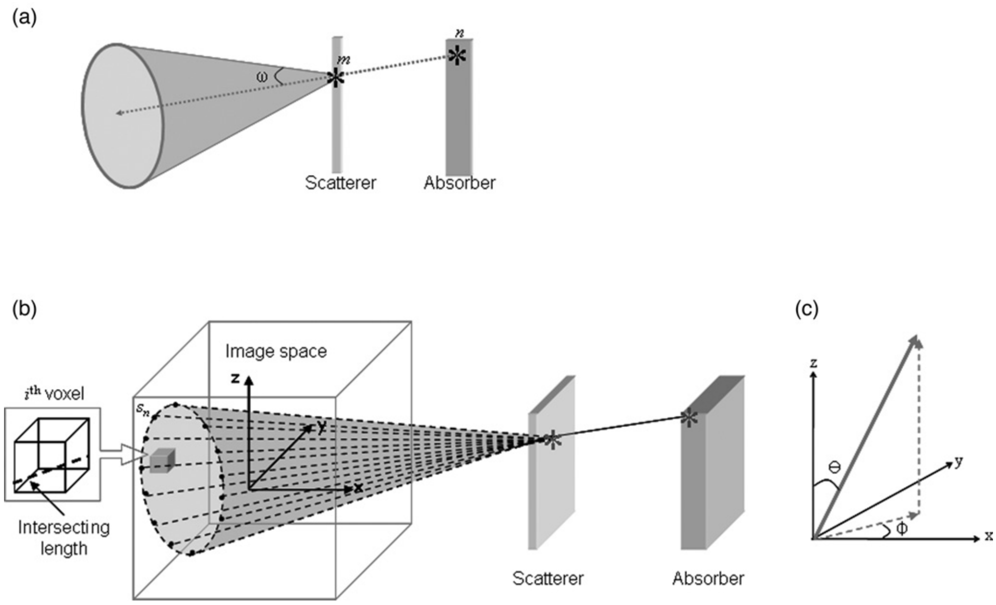

Figure 1. (a) A configuration of a typical Compton camera and representation of the conical ambiguity (ω is a SA, and m and n are the DPs in the scatterer and the absorber, respectively). (b) The conical surface integral calculated using the ray-tracing method. (c) The azimuthal and the polar angles, θ and φ, in spherical coordinates.

improving quantitative accuracy in Compton camera reconstruction (Hebert *et al* 1990, Sauve *et al* 1999). In fact, although the current application of EM reconstruction to Compton imaging may be a difficult problem due to computational limitations, increases in computer speeds are sure to have a practical impact.

We note particularly that the well-known ordered subset (OS) principle in tomographic image reconstruction is an algorithmic acceleration method that achieves faster convergence rates than non-OS statistical reconstruction algorithms. The standard EM algorithm uses the estimation of all projections and calculates the ratios between estimated and measured values for all projections during the backprojection process, whereas the OSEM algorithm first subdivides projection data into several subsets and then progressively processes each subset of projections by calculating projection and backprojection during each iteration (Hudson and Larkin 1994). As the OS level (number of subsets) increases, the OS procedure accelerates convergence by a factor proportional to the OS level. We also note that no systematic study of OSEM has contributed to a significant computational improvement for Compton cameras, although previously OS reconstruction has been applied to the 3D problem of Compton imaging based on splitting list-mode data into a number of subsets. However, these reconstructions do not demonstrate faster convergence rates than non-OS algorithms (Kragh 2002).

Since the form of the EM algorithm is the same for all emission imaging systems, the EM algorithm for Compton camera reconstruction can also be implemented with the familiar procedure for conventional ECT. However, the OSEM procedure used for Compton camera reconstruction is quite different from that used for conventional ECT, such as single photon emission computed tomography (SPECT) or positron emission tomography (PET), because grouping the Compton scattered data into OS is determined by both SA and DP pairs in the scatterer and the absorber. In this paper, we focus on the development of efficient methods for grouping Compton scattered conical projection data into OS. The remainder of the paper formulates the OSEM algorithm for Compton camera reconstruction, describes the details on how to construct OS and presents our experimental results.

2. Materials and methods

2.1. OSEM reconstruction algorithm

Recently, emphasis has been placed on accelerating iterative tomographic reconstruction methods that can produce an image with less iteration than the EM algorithm. In terms of the problem of ECT image reconstruction, the OSEM algorithm, proposed by Hudson and Larkin (1994), has been successful at accelerating the existing EM algorithm, and is continually increasing in its popularity. This is presumably due to the fact that while retaining the advantages of the existing EM algorithm, such as the accurate modeling of any type of system, OSEM provides an order-of-magnitude acceleration over EM.

Since the scheme of the EM algorithm is the same for all emission imaging systems, the EM algorithm for Compton camera reconstruction can be implemented using the procedure used for conventional ECT (Hebert *et al* 1990, Shepp and Vardi 1982, Lange and Carson 1984). In fact, the principle of OS can be applied to any algorithm that involves the calculation of a sum over projection indices; an OS version of the algorithm can be obtained by replacing the sums over all projection indices with sums over subsets (or blocks) of data. For a Compton camera, projection indices indicate the locations of DP pairs in the scatterer and the absorber, and SA. Therefore, for constructing subsets, the projection data can be grouped according to the DP pairs and the SA indexed by m, n and ω.

In this paper, we consider three different ways of grouping the projection data into OS. The first involves grouping data according to a pre-set order of SA. The second involves grouping the possible combinations of DP pairs in the scatterer and the absorber, and the third involves combining the first and second methods (referred to as AP (angles and positions)). The outline for OSEM applied to Compton camera reconstruction is then as follows:

For each iteration $k = 0, \ldots, K-1$
  For subsets grouped by scheme 1 $a = 0, \ldots, A-1$
    For subsets grouped by scheme 2 $b = 0, \ldots, B-1$
      · $j = (a \times B) + b$
      · jth subset $S_j = (S_a, S_b) = \{m, n, \omega\}$
      · Projection: $g_{mn\omega}^{(k,j)} = \sum_i H_{i;mn\omega} f_i^{(k,j)}$
      · Backprojection: $\sum_{mn\omega} H_{i;mn\omega} \frac{g_{mn\omega}}{g_{mn\omega}^{(k,j)}}$
      · Update voxels using $f_i^{(k,j+1)} = \frac{f_i^{(k,j)}}{\sum_{mn\omega} H_{i;mn\omega}} \sum_{mn\omega} H_{i;mn\omega} \frac{g_{mn\omega}}{g_{mn\omega}^{(k,j)}}$
    END
  END
END

In the above procedure, f_i is the ith voxel value in the 3D reconstructed image, and $g_{mn\omega}$ are the detected counts at the projection bin indexed by (m, n, ω). $H_{i;mn\omega}$ is an element of the system matrix that represents the probability that a photon emitted from the ith voxel will hit the detector bin indexed by (m, n, ω). The grouping schemes 1 and 2 stand for the SA-based scheme and the DP-based scheme, respectively. One can choose either one of these two schemes or both. When both schemes are combined (AP) as shown above, the total number of subsets used becomes $A \times B$.

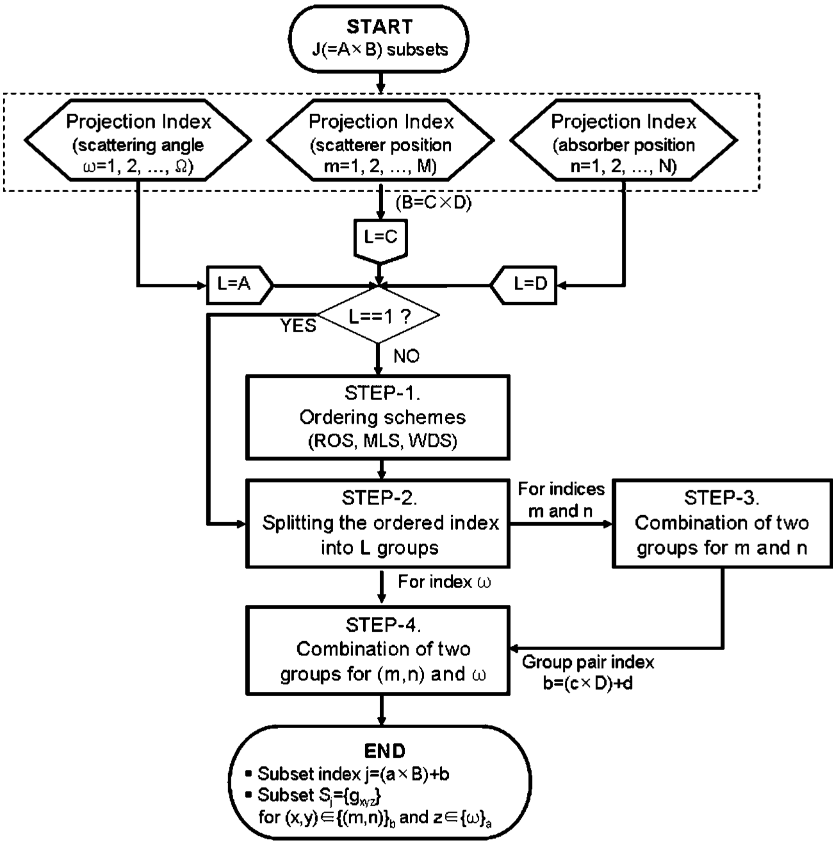

Figure 2. The outline of the procedure used for constructing subsets according to SA and DP pairs.

2.2. *Subset construction methods*

In the OSEM algorithm, subsets are usually chosen in a balanced way such that voxel activity contributes equally to any subset. Because it is best to order the subsets such that two adjacent indices for projection angles in a given subset correspond to the actual angles of the maximum angular distance (Hudson and Larkin 1994), we used this strategy for our conical projection data formed by the locations of DP pairs and SA.

The AP scheme, which is a method that combines both SA- and DP-based subset construction methods, is explained diagrammatically in figure 2. Using the measured SA and DP pairs, the conical projection data $g_{mn\omega}$ were divided into J well-balanced subsets. Each projection index, ω $(= 1, \ldots, \Omega)$, m $(= 1, \ldots, M)$ and n $(= 1, \ldots, N)$, was separately ordered and split into L groups through STEP-1 and STEP-2 in figure 2. (The manner in which projection index is ordered will be explained in the next section.) Additional possible combinations of two groups relating to the DPs m and n were performed to construct B DP group pairs $\{(m, n)\}_{b;b=1,\ldots,B}$ (STEP-3 in figure 2). Finally, as shown in STEP-4, J $(=A\times B)$ subsets were constructed as the possible combination of A SA group $\{\omega\}_{a;a=1,\ldots,A}$ and B DP group pairs $\{(m, n)\}_{b;b=1,\ldots,B}$. For example, the jth subset S_j contains all conical projection data indexed by (x, y, z) for $(x, y) \in \{(m, n)\}_b$ and $z \in \{\omega\}_a$.

In the SA scheme, indexing the conical projection data by using SA is similar to indexing parallel projection data using projection angles for conventional ECT. When the conical projection data are sorted only according to SA, two adjacent indices in a given subset correspond to the actual angles with the maximum angular distance. In the SA-based procedure used to group the conical projection data into OS, the number B of DP group pairs is set to one, and STEP-1 is skipped for m and n. The number of subsets J corresponds to the SA-group number A, and after STEP-4 in the SA scheme, the jth subset contains the projection data representing all possible DPs and $\{\omega\}_j$, which is reorganized through STEP-1 to STEP-4.

An incident angle on the detector could be determined by the axes connecting the DPs m and n in the scatterer and the absorber as well as the SA. In the DP scheme, similar to the SA scheme, the SA-group number A is set to one and STEP-1 for ω is skipped. Through STEP-1 and STEP-2 in figure 2, the DPs m and n were aligned separately according to the ordering scheme, which will be explained later, and then divided into C and D groups, respectively. J is the same as the DP-group pair number B, which is a combination number of $C \times D$. The jth DP-based subset consisted of the projection data representing all measurable SA and $\{(m, n)\}_j$.

2.3. Order selection schemes for subset construction

In contrast to the EM algorithm, the OSEM algorithm back-projects iteratively the error between measured and estimated projection data in a subset into the image space to update voxel intensity. Accordingly, the quality of a reconstructed image is affected by the projection data chosen to construct a subset, which is related to the ordering scheme used. Thus, we compared three different ordering schemes to construct subsets that are balanced in such a way that voxel activity contributes equally to any subset: random ordering scheme (ROS), multilevel ordering scheme (MLS) and weighted-distance ordering scheme (WDS).

In the ROS, the projection data (the set of cones determined by DP pairs and SA) were randomly chosen from the unselected cones using a random number generator with a uniform distribution. The selected order through the ROS is fixed during OSEM reconstruction. Since the angular or positional distance determined by the ROS differs each time, it does not offer a reproducible means of obtaining OSEM results.

In the MLS, ordering is related to the levels $L = 1, 2, \ldots, \log_2 M$, where M is the total number of cones to be ordered (Guan and Gordon 1994). At each level L, new cones were determined by adding $M/2^L$ to all indices of the chosen cones at previous levels ($<L$). The MLS is a traditional method used in OSEM for the ECT system, and is regarded as a proper scheme for ordering data according to angles.

The WDS is another method that was proposed to construct optimal subsets in the OSEM algorithm for SPECT or PET (Mueller *et al* 1997). According to this scheme, a new cone is chosen that has the maximum distance from the previously chosen cones, as shown in figure 3. The greater distance between the cones indicates that the cones can cover the wider field-of-view to be reconstructed. In the Compton camera, we can define two different types of distances: angular and positional distances. The angular distance is the difference between the SA of two cones. Similarly, the positional distance is the difference between the detection positions, which determine the axes of the cones. As shown in figure 3, the WDS calculates the weighted mean of repulsive force and the standard deviation (SD) of the distances between the cones selected previously in set B and the newly selected cone from set A through STEP-1 and STEP-2. The repulsive forces in the SA and DP grouping schemes are inversely proportional to the angular and positional distances, respectively. Different weights are applied to the pre-selected cones in set B. Finally, by minimizing the weighted mean and SD of repulsive

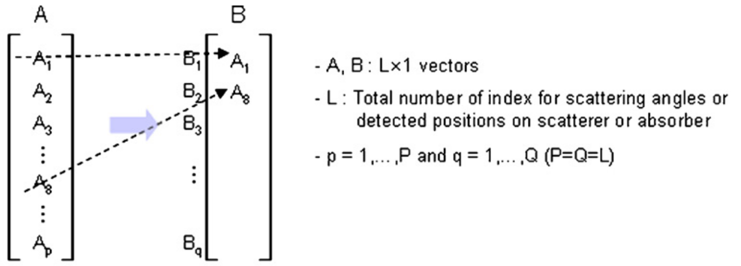

STEP-1) Weighted mean μ_p of the "repulsive forces" : $\mu_p = \sum_{q=0}^{Q-1} \omega_q d_{pq} \Big/ \sum_{q=0}^{Q-1} \omega_q$

- Weight : $\omega_q = \dfrac{q+1}{Q}$

- Angular distance : $d_{pq} = 1 \big/ \mathrm{Min}\left(\left|\omega_p - \omega_q\right|, L - \left|\omega_p - \omega_q\right|\right)$

- Positional distance : $d_{pq} = d_{\max} - \left|A_p - B_q\right|$

STEP-2) Weighted SD σ_p of the angular or positional distance :

$$\sigma_p = \sqrt{\sum_{q=0}^{Q-1} \omega_q \left(d_{pq} - \bar{d}_p\right)^2 \Big/ \sum_{q=0}^{Q-1} \omega_q}$$

STEP-3) Select an A_p to minimize N_p and insert A_p into B : $N_p = \mu_p^2 + 0.5\sigma_p^2$

Figure 3. Summary of the WDS to align projections according to SA or DPs.

forces between cones indexed by p and q (STEP-3), the WDS can rearrange set A into set B, which provides the maximum mean distance between the cones.

2.4. System matrix

In our model of the Compton camera, each element $H_{i;mn\omega}$ of the system matrix was factorized into two components: the belonging probability $P(m, n|i, \omega)$ of the ith voxel on the conical surface, defined by (m, n, ω), and the Compton scattering probability $P(\omega)$ of the SA ω, as given by

$$H_{i;mn\omega} \approx P(m, n|i, \omega) P(\omega). \tag{1}$$

The probability $P(\omega)$ in the above equation is the differential cross-section for the Compton scattering interaction with matter. In this study, this probability was expressed using the Klein–Nishina formula based on the assumption that the electrons were at rest (Weinberg 1995). Because the differential cross-section is a function of the SA ω, $P(\omega)$ can be calculated using the ratio of the corresponding area of the sampled range for a discrete SA ω to the total area under the curve.

The belonging probability $P(m, n|i, \omega)$ was approximated to the intersecting length of the voxel and the sampled rays passing through the apex on the conical surface using a ray-tracing method (Kim *et al* 2007), as shown in figure 1(b). In order to sample a given conical surface into rays, we first defined a reference cone (RC) with the same SA as a given cone.

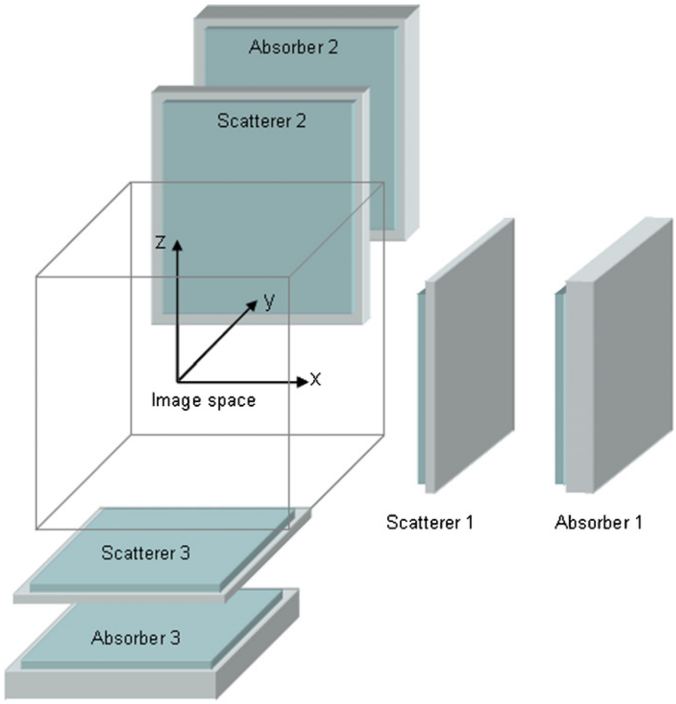

Figure 4. The Compton camera system with three detector pairs of the scatterer and the absorber used for simulation purposes.

The apex and the conical axis of the RC were placed on the origin and the x-axis of the image space, respectively. The circumference of the base of the RC was then evenly sampled. The total number of sampled points (s_n in figure 1(c)) on the circumference was fixed at 120. The sampled points on the circumference were transformed using the interaction position on the scatterer and the rotating angles θ and φ. The rotating angles θ and φ are the polar angle from the z-axis and the azimuthal angle in the xy-plane from the x-axis in spherical coordinates, respectively. θ and φ were determined using the direction vector of the axis of a given cone. Finally, the sampled rays on the given conical surface were obtained by connecting the apex of the given cone and the transformed sampled points on the base circumference of the RC. Using Siddon's method (Siddon 1985), the intersecting lengths of voxels and the sampled rays on the given conical surface were efficiently calculated.

2.5. Experimental conditions

In this study, to alleviate the limited-angle problem involved in a typical Compton camera system, which consists of a single detector pair, we designed a Compton camera system consisting of three detector pairs perpendicular to each other, as shown in figure 4. Each detector pair was placed on the x-, y- and z-axes with a radial offset of 10 cm from the center of the image space. The distance between the scatterer and the absorber for each detector pair was 5 cm. The measured data were binned according to DPs and SA. The DPs in the scatterer and the absorber were sampled into 16×16 discrete positions, and the areas of

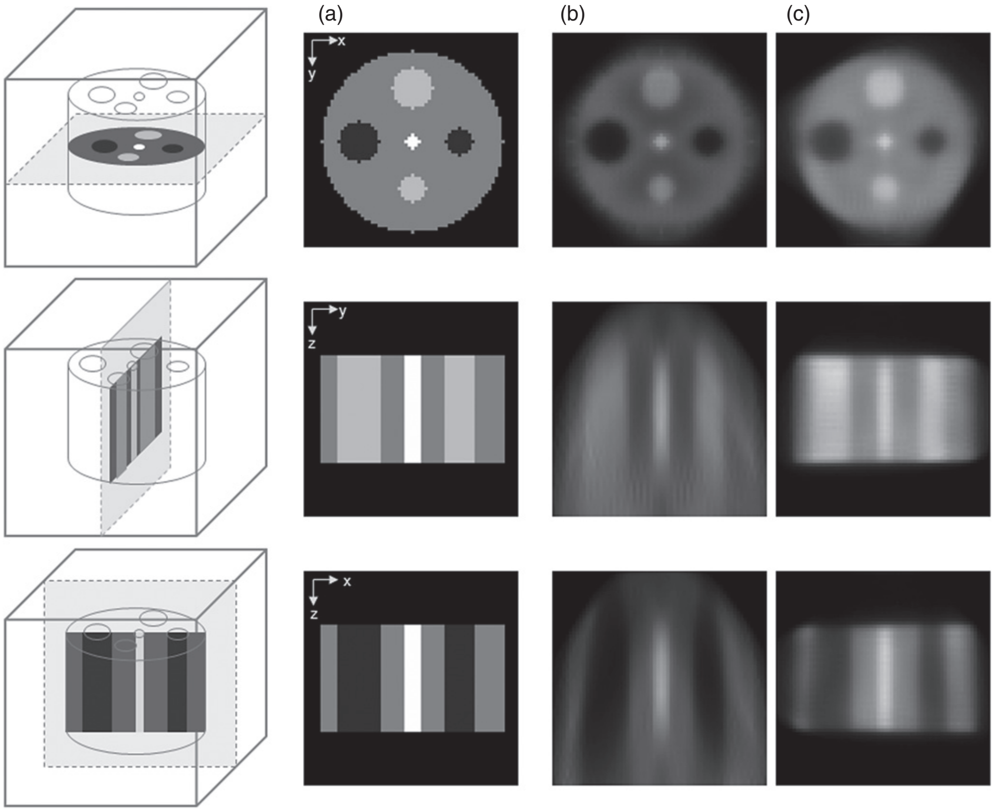

Figure 5. The *xy*-, *yz*- and *xz*-central planes of the original six-cylinder phantom, and EM reconstructions for data obtained using single (1-DIR) and triple (3-DIR) detector pairs: (a) six-cylinder phantom, (b) 1-DIR geometry and (c) 3-DIR geometry.

detector elements on both detectors were 3.125×3.125 mm^2. The SA of the incident photon at the scatterer were grouped into 32 discrete angles between 10° and 90°.

We used two mathematical phantoms, a six-cylinder phantom and a uniform cubic phantom, as shown in figures 5 and 8, respectively. The six-cylinder phantom, which is a cylinder with a diameter of 8.4 cm and a length of 5 cm, contained five cylinders with various diameters and voxel values. The uniform cubic phantom had a width and a height of 5 cm each, and it was uniformly distributed with a value of 1. Both phantoms were located at the center of a $10 \times 10 \times 10$ cm^3 3D image space. The image space was represented using a $64 \times 64 \times 64$ (voxel) image matrix and a voxel size of $1.56 \times 1.56 \times 1.56$ mm^3. The three directional projection data of the two phantoms emitting gamma rays of 511 keV were obtained from our projector modeled for a Compton camera.

We implemented the OSEM algorithms with nine different combinations of three subset constructions and three ordering schemes with an OS level of 16 and an iteration number of 16. For example, the 16 DP-based subsets were constructed using combinations of four pre-defined position groups in the scatterer and four groups in the absorber, as described in STEP-3 of figure 2. In the case of the AP-based scheme, the subsets were formed by all possible combinations of four (scatterer) and two (absorber) position groups and two SA

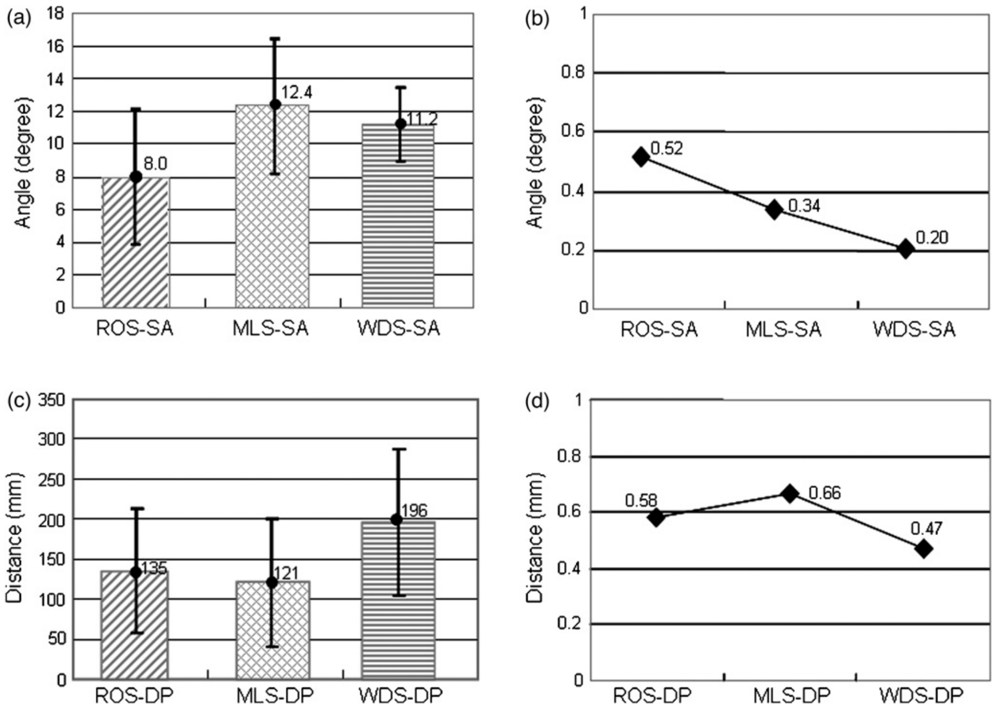

Figure 6. Graphs of means ± SDs and CVs of angular and positional differences calculated using the ordered sequences of the different ordering schemes: (a), (b) means ± SDs and CV graphs for SA-based ordering; (c), (d) means ± SDs and CV graphs for DP-based ordering.

groups. For comparison with the OSEM algorithm, the EM algorithm was also performed using 256 iterations.

To compare the three ordering schemes (ROS, MLS and WDS) the coefficients of variation (CVs) were calculated as defined by the ratio of the SD to the mean of angular and positional differences between two adjacent indices of SA and DP pairs. The smaller CV of the angular and positional differences is also necessary to compose a well-balanced subset because differences between data in a given subset should also be uniform to minimize information redundancy. In the case of the uniform cubic phantom, the CVs of OSEM reconstructions were calculated for the nonzero uniform region of the phantom. In addition, the percentage errors between the original phantom and reconstructed images were calculated as follows:

$$\mathrm{PE} = \sqrt{\frac{\sum_i (\hat{f}_i - f_i)^2}{\sum_i f_i^2}} \times 100(\%). \tag{2}$$

We also performed EM and OSEM reconstructions for noisy Compton projection data to test the stability of OSEM algorithms with respect to the OS levels. In order to generate noisy data for the six-cylinder phantom, Poisson random noise was added to the projection data. Assuming a total source activity of 3 mCi for the six-cylinder phantom, a detector pair sensitivity of 8×10^{-6} and an acquisition time of 30 min, the total detected counts were approximately 4.8×10^6. EM was performed using 256 iterations. The OS levels of 16, 32, 64 and 128 were tested for DP- and AP-based OSEMs with the three different ordering schemes. The corresponding iteration numbers for the chosen OS levels were 16, 8, 4 and 2,

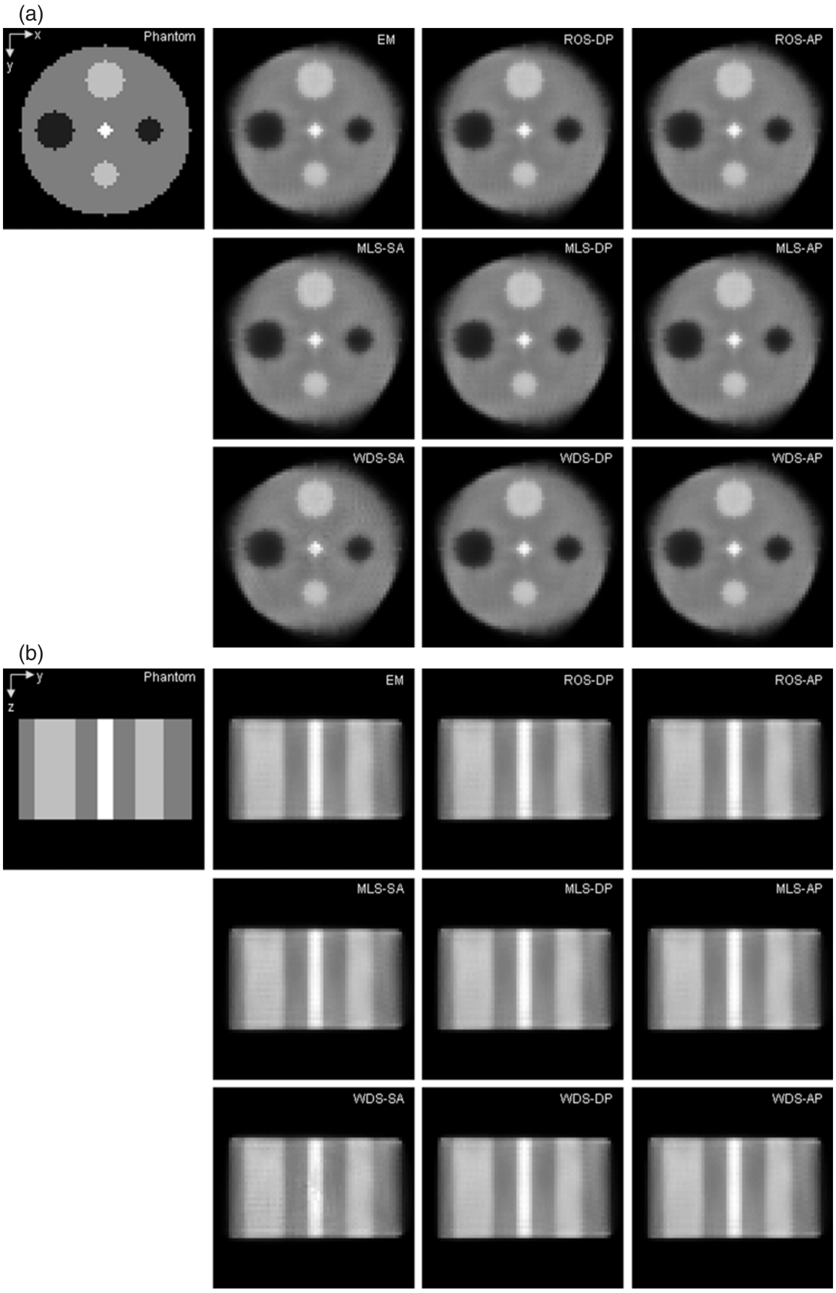

Figure 7. The central planes and percentage error graph of the original six-cylinder phantom, EM (256 iterations) and OSEM (16 subsets and 16 iterations) algorithms with different ordering schemes for noiseless data: (a) *xy*- and (b) *yz*-central planes and (c) percentage error.

(c)

EM	18.07 %		
	SA	DP	AP
ROS	134.7 %	18.09 %	18.07 %
MLS	18.73 %	18.11 %	18.11 %
WDS	18.98 %	17.82 %	17.84 %

Figure 7. (Continued.)

respectively. SA-based OSEM was performed using two, four and eight subsets due to the limited number of discrete SA. The corresponding iteration numbers were 128, 64 and 32, respectively. The percentage errors were calculated after 3D Gaussian post-filtering with a full width at half maximum (FWHM) of 4 mm for all reconstructed images by equation (2).

3. Results

3.1. Geometric comparisons

In this study, we designed a geometry consisting of three detector pairs (3-DIR) (figure 4), which provided a wider angular coverage of the field of view than the traditional camera consisting of one detector pair (1-DIR). Figure 5 compares the EM (64 iterations) results for noiseless data obtained using the 1-DIR and 3-DIR geometries. Figures 5(a), (b) and (c) show orthogonal planes on the x-, y- and z-axes of the six-cylinder phantom and the 3D EM images for the 1-DIR and 3-DIR geometries. As compared with the traditional 1-DIR geometry, 3-DIR resulted in much improved reconstruction accuracy. Computation times were almost same due to the geometric symmetry regarding the perpendicular relationship between 1-DIR and 3-DIR.

3.2. Comparison of subset constructions and ordering schemes

Figure 6 shows the graphs of means ± SDs and CVs of the angular and positional differences calculated using each of the ordering schemes. The MLS and WDS provided the largest mean differences for the SA- and DP-based ordering schemes, respectively. A larger mean difference in ordered data means that data are ordered in a well-balanced manner. In contrast, the WDS provided lowest CVs for both SA- and DP-based ordering schemes. These lower CVs indicate an improved capability of ordering projection data and more uniform differences between two adjacent projections.

Figures 7 and 8 show the results obtained from tests using noiseless data. Figure 7 shows the results obtained using the 3D EM and OSEM reconstructions, whereby projection data generated from the six-cylinder phantom were divided into 16 subsets using the different subset constructions and ordering schemes. The iteration number used for the EM and OSEM algorithms were 256 and 16, respectively. In this comparative analysis, the results generated using OSEM-ROS-SA were excluded, because it caused a significant artifact on the reconstructed images.

Figures 7(a) and (b) show orthogonal slices of the xy- and yz-planes of the phantom and the 3D reconstructed images. The percentage errors shown in figure 7(c) were calculated

(a)

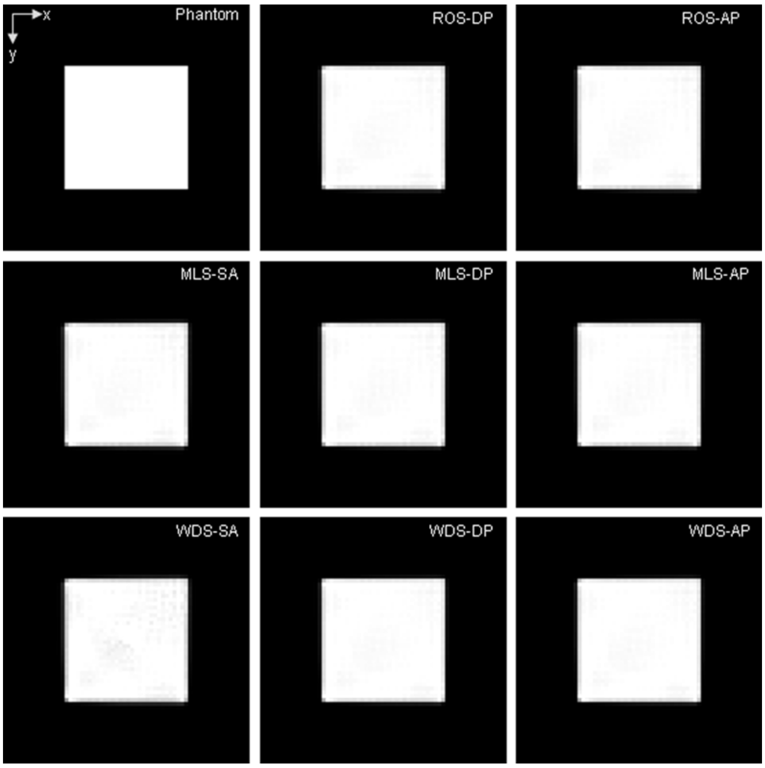

(b)

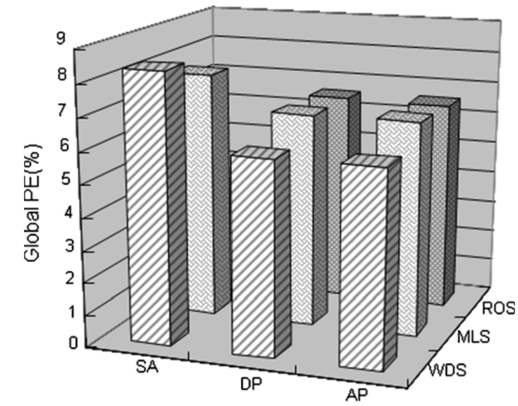

	SA	DP	AP
ROS	62.8	6.59	6.57
MLS	7.71	6.67	6.69
WDS	8.37	6.03	6.06

Figure 8. The *xy*-central planes, graphs of percentage errors and uniformities for the original uniform cubic phantom and the OSEM algorithm with different ordering schemes for noiseless data: (a) *xy*-central planes, (b) percentage errors and (c) uniformity graph.

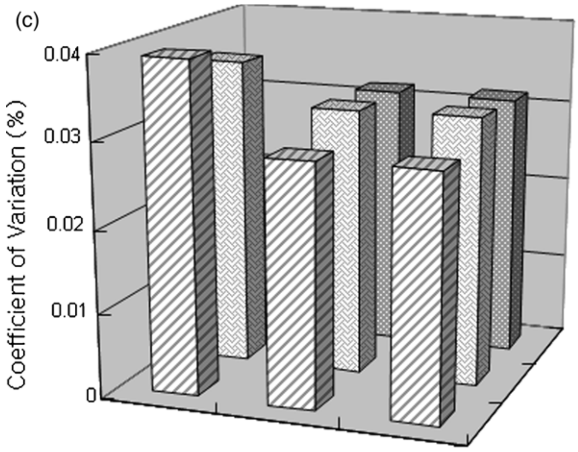

	SA	DP	AP
ROS	0.353	0.032	0.032
MLS	0.037	0.032	0.032
WDS	0.039	0.029	0.029

Figure 8. (Continued.)

using the formula mentioned in section 2.5. Little difference was observed qualitatively and quantitatively between the EM and OSEM results, as shown in figure 7. In the Linux system using an AMD Athlon X2 2.2 GHz CPU, total computation times for EMs and OSEMs were 3.5 days and 8.84 h (on average), respectively. All OSEM algorithms with different subset constructions and ordering schemes, except for the ROS-SA, produced reasonable reconstructed images and the rate of acceleration was proportional to the rate of increase in the number of subsets. DP- and AP-based OSEM methods provided lower errors than SA-based methods (figure 7(c)). The WDS provided the lowest percentage errors for the DP- and AP-based schemes, though these were only slightly lower than the errors of the other methods. No difference in total computation time was observed for all OSEM algorithms because the same number of subsets were used.

Figures 8(a), (b) and (c) show the average *xy*-planes, the percentage errors and the CVs for OSEM reconstructions with 16 subsets and 16 iterations using the uniform cubic phantom, respectively. The percentage errors showed the same trend as was observed for the six-cylinder phantom (figure 8(b)). To quantify uniformity in reconstructed images, CVs were calculated within the reconstructed volume, which corresponded to the nonzero region of the uniform cubic phantom. OSEM-ROS-SA provided the poorest uniformity (over 0.4%), and the others provided similar CVs of 0.02 to 0.04% (figure 8(c)).

3.3. Stability testing of the OSEM algorithm

In addition, we tested the stability of the OSEM algorithm using different ordering schemes with respect to the various OS levels using noisy Compton projection data. Figures 9–11 show the analysis results obtained using the SA-, DP- and AP-based OSEM reconstructions,

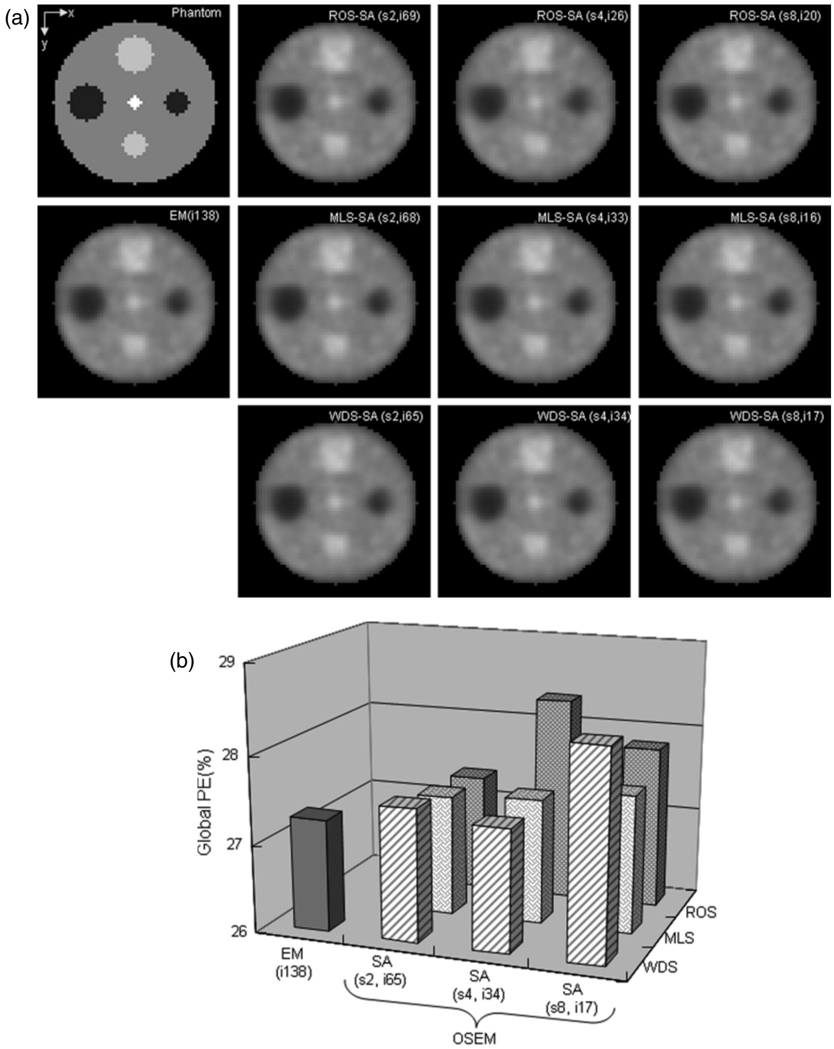

EM	27.28		
	SA (s2)	SA (s4)	SA (s8)
ROS	27.34	27.30	28.34
MLS	27.37	27.53	27.43
WDS	27.50	27.39	28.35

Figure 9. The average planes and percentage errors of OSEM-SA results from noisy data of the six-cylinder phantom: (a) average *xy*-planes, (b) lowest percentage errors for OSEM which were tested for the three ordering schemes and two, four and eight subsets, and (c) percentage error versus iteration plot for EM and OSEM-MLS with eight subsets and 32 iterations (in the plot, labels on the *x*-axis should be multiplied by 8 for the EM algorithm).

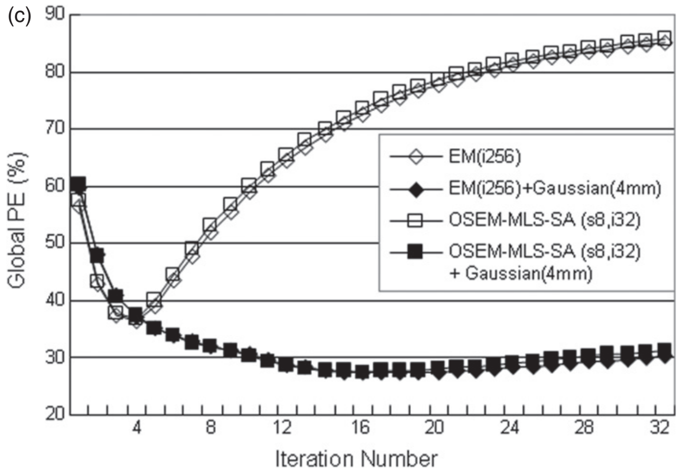

Figure 9. (Continued.)

respectively, and different number of subsets for noisy data. In these three figures, (a) and (b) show the average planes and the percentage errors of the EM and OSEM algorithms with different numbers of subsets and ordering schemes when the percentage errors were lowest during the iteration. Average planes were obtained from reconstructed transverse images corresponding to 32 planes perpendicular to the z-axis within a length of 5 cm. The effects of OSEM of increasing number of subsets on peripheral transverse images and on the central image can be observed simultaneously. The percentage errors of EM (256 iterations) and OSEM before and after applying a Gaussian smoothing filter are shown in (c), which confirm the order-of-magnitude acceleration achieved using the OSEM algorithm.

In figure 9(c), SA-based OSEM (eight subsets and 32 iterations) with the MLS ordering scheme is compared with EM with respect to percentage errors. For DP- and AP-based subset constructions, OSEM-WDS with 16 subsets and 16 iterations was compared with EM in (c) of figures 10 and 11. For this noisy data, OSEM provided images comparable to those provided by EM and stable images, although the subset number was increased. In particular, the MLS was the best choice for SA-based OSEM. On the other hand, DP- and AP-based OSEMs with the WDS ordering scheme worked well despite the increase in the number of subsets.

4. Discussion

In this study, in order to develop an OSEM algorithm for a Compton camera, an efficient projector and backprojector were modeled using the Compton scattering probability as determined using the Klein–Nishina formula, and the belonging probability as determined by the ray-tracing method. Since all cones for Compton scattered data were defined by an axis connecting two DPs in the scatterer and the absorber and a SA, we proposed three different subset construction methods, SA, DP and AP schemes. To achieve the maximum angular and positional differences between projections in a subset, we considered three ordering methods, namely ROS, MLS and WDS. These different approaches were then quantitatively compared.

Figure 5 shows a Compton camera comprising two planar detectors that views the object from only one side, and which suffers from typical limited-angle tomography artifacts e.g.

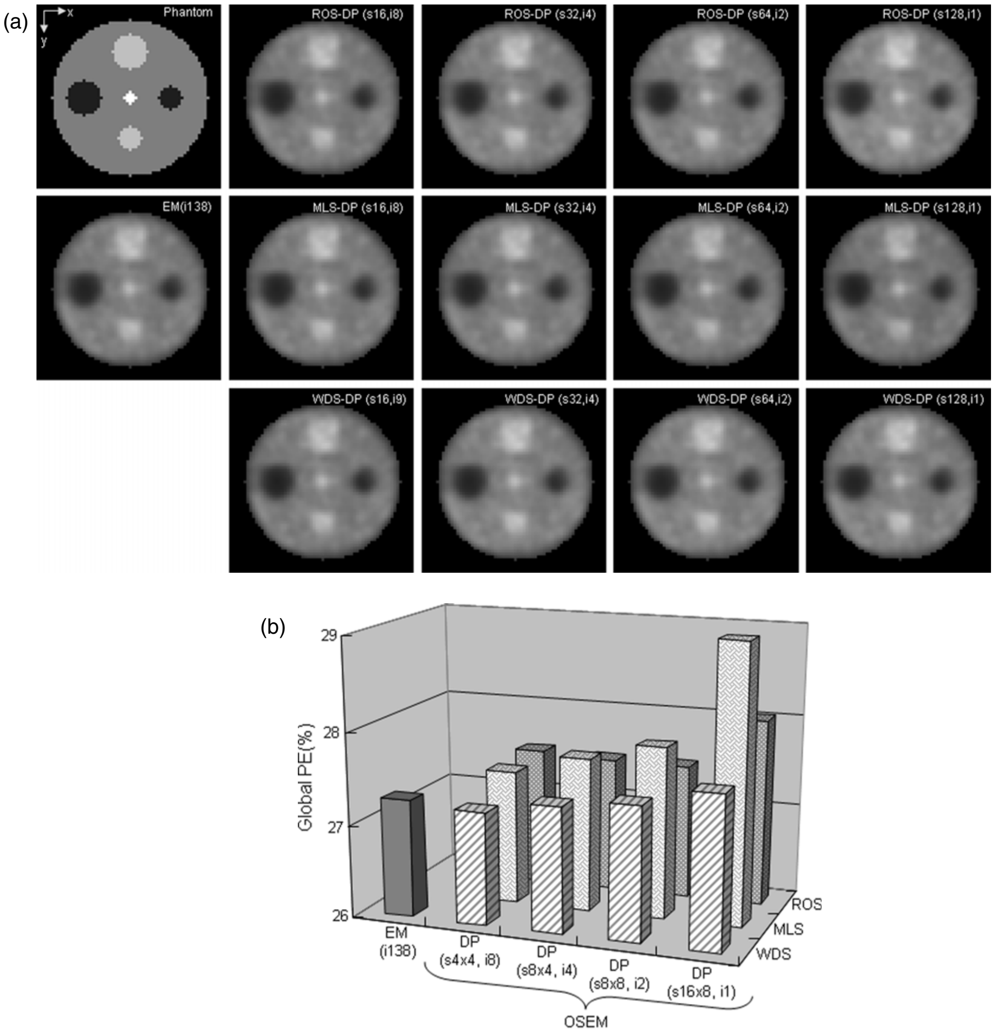

EM	27.28			
	DP (s4x4)	DP (s8x4)	DP (s8x8)	DP (s16x8)
ROS	27.50	27.47	27.46	28.03
MLS	27.45	27.66	27.85	29.02
WDS	27.22	27.36	27.45	27.64

Figure 10. The average planes and percentage errors of OSEM-DP results from noisy data of the six-cylinder phantom: (a) average *xy*-planes, (b) lowest percentage errors for the OSEM algorithm tested using the three ordering schemes and 16, 32, 64 and 128 subsets, and (c) percentage error versus iteration plot for the EM algorithm with 256 iterations, and for the OSEM-WDS algorithm with 16 subsets and 16 iterations (in the plot, the labels on the *x*-axis should be multiplied by 16 for the EM algorithm).

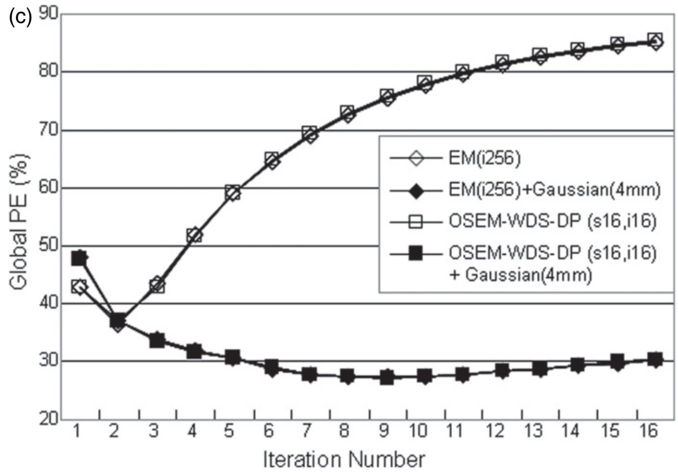

Figure 10. (Continued.)

poor depth resolution. However, a Compton camera consisting of more detector pairs (like the three detector pairs shown in figure 4) provides more complete tomographic sampling, and hence fewer artifacts are produced during reconstruction. To obtain compatible images using conventional molecular imaging systems various technical improvements, such as rotating Compton camera, would be required (Hua *et al* 1999, Sauve *et al* 1999, Smith 2005).

On one hand, the MLS and WDS methods resulted in maximum mean differences between two adjacent projections in the SA- and DP-based subset construction schemes, respectively. On the other hand, best uniformities of differences were obtained using the WDS method in both the SA and DP schemes. Based on the simulated results, we were able to compare the acceleration magnitude of the OSEM and EM algorithms. ROS-SA-based OSEM using more than eight subsets yielded artifactual results. For noisy data, all OSEM algorithms with other ordering schemes did not generate artifacts in the reconstructed images and showed good stabilities in terms of percentage errors, despite the increase in the number of subsets. In terms of OSEM for ECT, since the projection data were divided into OS according to the projection angles of gamma rays reaching the scintillation detector, a limited number of subsets were used. However, since OSEM for a Compton camera employed many more subsets, due to a combination of DP pairs and SA, it can provide more accelerated convergence if the data have good counting statistics. When we used 128 subsets for DP- and AP-based OSEMs, the reconstruction time was reduced to 1.2 h. As compared with other schemes, the MLS and WDS with proper number of subsets yielded better OSEM results for the SA and DP schemes than other combinations of subset constructions and ordering schemes. The three AP-based ordering schemes produced similar results using the DP schemes.

The proposed three ordering schemes used in this study could be applied to reconstruction using list-mode data from a Compton camera. Since each list-mode event in the data stream is detected randomly, the ROS can be easily applied. If the DP pair and the SA of each event are treated like continuous detection variables, the MLS and WDS ordering schemes could also be used for OSEM on list-mode data.

In this study, we computed the Compton scattering probability without taking into account the Doppler broadening effect. In the future, we will consider a more realistic system model for quantitative reconstruction. This system model will include the Compton scattering probability

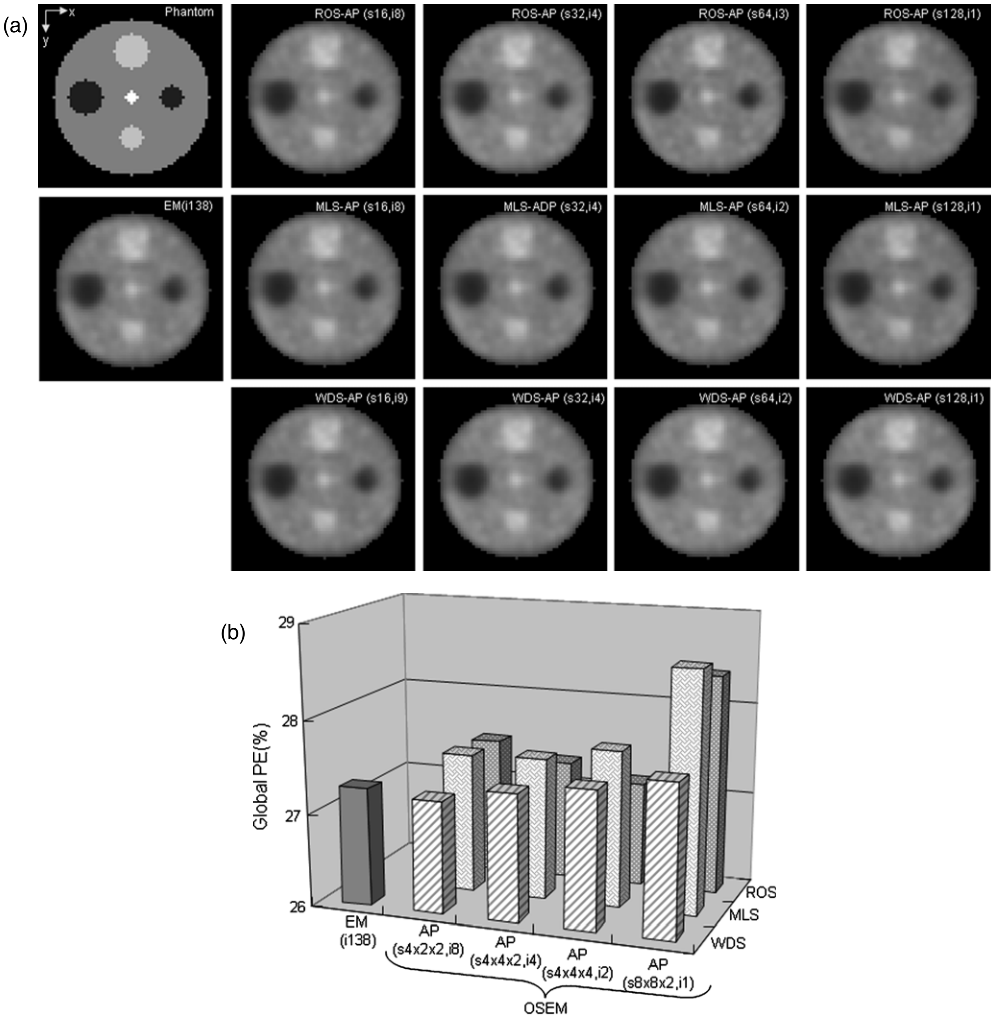

EM	27.28			
	AP (s4x2x2)	AP (s4x4x2)	AP (s4x4x4)	AP (s8x8x2)
ROS	27.49	27.30	27.14	28.38
MLS	27.51	27.53	27.69	28.60
WDS	27.21	27.37	27.48	27.65

Figure 11. The average planes and percentage errors for OSEM-AP results from noisy data of the six-cylinder phantom: (a) average *xy*-planes, (b) lowest percentage errors for the OSEM algorithm tested using the three ordering schemes and 16, 32, 64 and 128 subsets, and (c) percentage error versus iteration plot for the EM algorithm using 256 iterations and for the OSEM-WDS algorithm with 16 subsets and 16 iterations (in the plot, the labels on the *x*-axis should be multiplied by 16 for the EM algorithm).

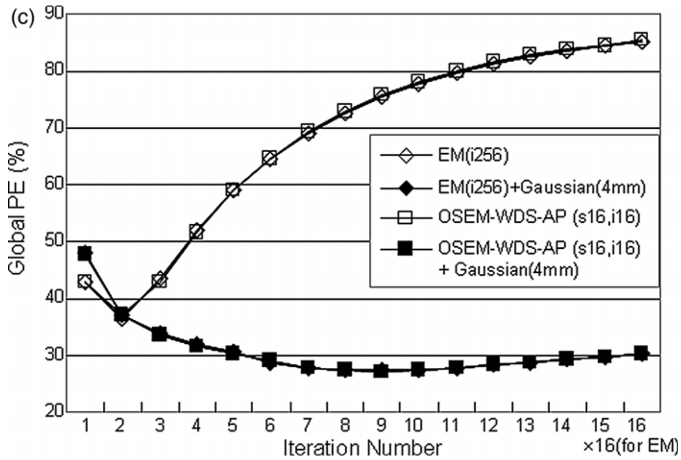

Figure 11. (Continued.)

including uncertainties on SA caused by Doppler broadening and energy resolution. We expect that correction for Doppler broadening can be performed during OSEM reconstruction implemented by a realistic system model. Since the computational burden would be markedly increased by a more sophisticated system model, the use of multi-core processors and GPUs would be required for parallel processing for image reconstruction (Ha *et al* 2009, Park *et al* 2009).

5. Conclusion

In this study, the OSEM algorithm was applied to a Compton camera employing electronic collimation to reconstruct Compton scattered data. In order to construct subsets for the OSEM algorithm, we proposed combinations of three subset construction methods (SA, DP and AP schemes) and three ordering schemes (ROS, MLS and WDS). The experimental results obtained showed that all OSEMs with different combinations of subset constructions and ordering schemes provided an order-of-magnitude acceleration and retained overall quality over the standard EM algorithm. The MLS and WDS provided maximum mean differences for the SA and DP schemes, respectively. In contrast, the WDS exhibited minimum CVs for both the SA and DP schemes. Furthermore, all OSEMs with different ordering schemes exhibited similar performances in terms of quantitative accuracy and computational efficiency. The MLS and WDS with appropriately chosen subsets yielded comparatively better OSEM results for the SA and DP schemes, respectively. Moreover, because the performance of the AP-based ordering schemes was intermediate to the performance of the SA- and DP-based schemes and can use a larger subset number, they would be usable for list-mode data including various SA. We expect that OSEM reconstruction will be found useful for Compton imaging as the OSEM algorithm for ECT when multi-core processors or GPUs are adopted.

Acknowledgment

This work was supported by the Nuclear Research & Development Program of the National Research Foundation of Korea (NRF) funded by the Ministry of Education, Science & Technology (MEST) (grant codes 2005-2004723, 2008-2003852).

References

An S H, Seo H, Lee J H, Lee C S, Lee J S and Kim C H 2007 Effect of detector parameters on the image quality of Compton camera for ^{99m}Tc *Nucl. Instrum. Methods Phys. Res.* A **571** 251–4

Basko R, Zeng G L and Gullberg G T 1998 Application of spherical harmonics to image reconstruction for the Compton camera *Phys. Med. Biol.* **43** 887–94

Guan H and Gordon R 1994 A projection access order for speedy convergence of ART (algebraic reconstruction technique): a multilevel scheme for computed tomography *Phys. Med. Biol.* **39** 2005–22

Ha W S, Kim S M, Park M J, Lee D S and Lee J S 2009 A study on GPU-based iterative ML-EM reconstruction algorithm for emission computed tomographic imaging systems *Nucl. Med. Mol. Imaging* **43** 459–67

Hebert T, Leahy R and Singh M 1990 Three-dimensional maximum-likelihood reconstruction for an electronically collimated single-photon-emission imaging system *J. Opt. Soc. Am.* A **7** 1305–13

Hirasawa M and Tomitani T 2003 An analytical image reconstruction algorithm to compensate for scattering angle broadening in Compton cameras *Phys. Med. Biol.* **48** 1009–26

Hua C H, Clinthorne N H, Wilderman S J, LeBlanc J W and Rogers W L 1999 Quantitative evaluation of information loss for Compton cameras *IEEE Trans. Nucl. Sci.* **45** 587–93

Hudson H M and Larkin R S 1994 Accelerated image reconstruction using ordered subsets of projection data *IEEE Trans. Med. Imaging* **13** 601–9

Kim S M, Lee J S, Lee M N, Lee J H, Lee C S, Kim C H, Lee D S and Lee S-J 2007 Two approaches to implementing projector–backprojector pairs for 3D reconstruction from Compton scattered data *Nucl. Instrum. Methods* A **571** 255–8

Kragh T J 2002 Tradeoffs and limitations in statistically based image reconstruction problems *PhD Thesis* University Michigan Ann Arbor, MI, USA

Lange K and Carson R 1984 EM reconstruction algorithms for emission and transmission tomography *J. Comput. Assist. Tomogr.* **8** 306–16

LeBlanc J W, Clinthorne N H, Hua C-H, Nygard E, Rogers W L, Wehe D K, Weilhammer P and Wilderman S J 1999 Experimental results from the C-SPRINT prototype Compton camera *IEEE Trans. Nucl. Sci.* **46** 201–4

Lee J H, Kim N Y, Lee C S and Jang Z H 2005 Development of the multi-purpose gamma-ray detection system consisting of a double-sided silicon strip detector and a 25-segmented germanium detector *Nucl. Phys.* A **758** 150c–3c

Lee J H and Lee C S 2006 Monte Carlo study on the imaging resolution and sensitivity of a Compton camera *J. Korean Phys. Soc.* **49** 97–102

Mueller K, Yagel R and Cornhill J F 1997 The weighted-distance scheme: a globally optimizing projection ordering method for ART *IEEE Trans. Med. Imaging* **16** 223–30

Park M J, Lee J S, Kim S M, Kang J Y, Lee D S and Park K S 2009 Preliminary study on the enhancement of reconstruction speed for emission computed tomography using parallel processing *Nucl. Med. Mol. Imaging* **43** 443–50

Parra L C 2000 Reconstruction of cone-beam projections from Compton scattered data *IEEE Trans. Nucl. Sci.* **47** 1543–50

Qi J and Leahy R M 2006 Iterative reconstruction techniques in emission computed tomography *Phys. Med. Biol.* **51** R541–78

Sauve A C, Hero A O, Rogers W L, Wilderman S J and Clinthorne N H 1999 3D image reconstruction for Compton SPECT camera model *IEEE Trans. Nucl. Sci.* **46** 2075–84

Seo H, Lee S H, Jeong J H, Lee J H, Lee C S, Lee J S and Kim C H 2008 AID—a novel method for improving the imaging resolution of a table-top Compton camera *IEEE Trans. Nucl. Sci.* **55** 2527–30

Shepp L A and Vardi Y 1982 Maximum likelihood reconstruction for emission tomography *IEEE Trans. Med. Imaging* **1** 113–22

Siddon R L 1985 Fast calculation of the exact radiological path for a three-dimensional CT array *Med. Phys.* **12** 252–5

Smith B 2005 Reconstruction methods and completeness conditions for two Compton data models *J. Opt. Soc. Am.* A **22** 445–59

Tomitani T and Hirasawa M 2002 Image reconstruction from limited angle Compton camera data *Phys. Med. Biol.* **47** 2129–45

Weinberg S 1995 *The Quantum Theory of Fields: Vol 1.Foundations* (Cambridge: Cambridge University Press)

Yang Y F, Gono Y, Motomura S, Enomoto S and Yano Y 2001 A Compton camera for multitracer imaging *IEEE Trans. Nucl. Sci.* **48** 656–61